



# Analysis of AM-to-PM conversion in MUTC photodiodes based on an equivalent circuit model

ZHENJIE SONG,<sup>1,2,6</sup>  ZHIQI ZHOU,<sup>2,3,4,6</sup> JIAN HUANG,<sup>2</sup> XINBO ZOU,<sup>2</sup> CHUN YANG,<sup>1,7</sup> AND BAILE CHEN<sup>2,5,8</sup> 

<sup>1</sup>National ASIC System Engineering Research Center, School of Electronic Science and Engineering, Southeast University, Nanjing 210096, China

<sup>2</sup>School of Information Science and Technology, ShanghaiTech University, Shanghai 201210, China

<sup>3</sup>Shanghai Institute of Microsystem and Information Technology, Chinese Academy of Sciences, Shanghai 200050, China

<sup>4</sup>University of Chinese Academy of Sciences, Beijing 100049, China

<sup>5</sup>Shanghai Engineering Research Center of Energy Efficient and Custom AI IC, Shanghai 201210, China

<sup>6</sup>These authors contributed equally to this work

<sup>7</sup>chunyang@seu.edu.cn

<sup>8</sup>chenbl@shanghaitech.edu.cn

**Abstract:** High-speed, high power-handling photodiodes with sufficiently low amplitude-to-phase (AM-to-PM) conversion coefficients are critical components in the systems that generate ultra-stable microwave signals. This paper reports the AM-to-PM conversion in modified uni-traveling carrier photodiodes (MUTC-PDs) with 20  $\mu\text{m}$  and 40  $\mu\text{m}$  diameters. The contributions of AM-to-PM conversions from the carrier transit-time and impedance were quantified systematically based on a photocurrent-dependent nonlinear equivalent circuit model. It is found that the AM-to-PM conversion in 40  $\mu\text{m}$  PD is dominated by the nonlinear impedance, while for 20  $\mu\text{m}$  PD, the transit-time impacts the AM-to-PM conversion more significantly. These results imply that, for large PDs, the nonlinearity of the PDs' photocurrent-dependent impedance is the critical reason causing AM-to-PM conversion.

© 2021 Optical Society of America under the terms of the [OSA Open Access Publishing Agreement](#)

## 1. Introduction

High-speed high-power photodiodes (PDs) are critical devices for microwave photonic applications such as opto-electronic oscillators [1,2], photonics-based coherent radar [3], photonic analog-to-digital convertor [4], and optical communications [5,6], which takes advantage of the large bandwidth and ultra-low phase noise of opto-electronically generated microwave signals. Among the noise sources, the electronic phase noise due to the conversion of relative intensity noise (RIN) of the laser can significantly deteriorate the timing precision of the microwave signals [7–11]. In many cases, this amplitude-to-phase (AM-to-PM) conversion can overwhelm the other noise sources in the microwave signal [12]. The AM-to-PM conversion coefficient  $\alpha$  has been characterized with microwave phase bridge and impulse response methods. It was found that there are AM-to-PM “null” points at some specific photocurrents, where this coefficient is zero [7–9,13,14]. Similar AM-to-PM behavior has also been reported in a silicon p-i-n photodiode [15]. In principle, operating at the “null” point of  $\alpha$  would be ideal for the photonic generation of low phase noise microwave signals which eliminates the dependence of phase noise on the RIN of a laser.

Theoretical studies on AM-to-PM conversion have been reported recently. Yue Hu et al. calculated the AM-to-PM conversion in a modified uni-traveling carrier PD (MUTC-PD) from Fourier transform of impulse response and attributed these “null” points to the nonlinear transit-time that changes with the average photocurrent [7]. X. Xie et al. experimentally investigated the

impact of nonlinear transit-time on AM-to-PM conversion without considering nonlinearities in the impedance on a 10  $\mu\text{m}$  diameter charge-compensated MUTC-PD [9,16]. Downscaling the diameter of the PD is essential to minimizing the impedance RC-time constant in order to boost the speed of the PD [17]. However, for the generation of high power and low-noise microwave signals, photonic systems require high power handling capability of the PD, which needs large diameter PD with low AM-to-PM conversion coefficient [18]. It has been found that phase change in PD originates from the nonlinear carrier transit time and device impedance dependency on photocurrent [16,19]. Therefore, an accurate PD model including nonlinear mechanisms of both carrier transit-time and impedance is necessary to understand and achieve a zero AM-to-PM conversion. To the best of our knowledge, no specific model including both effects has been reported on the AM-to-PM conversion.

In this paper, we studied the AM-to-PM conversion of MUTC-PDs with different diameters under various photocurrent and bias conditions. A photocurrent-dependent nonlinear equivalent circuit model including both carrier transit-time and impedance effects was used to fit the experimental results. We found that the AM-to-PM conversion of 40  $\mu\text{m}$  diameter PD originates mainly from nonlinear impedance dependency on photocurrent, while for 20  $\mu\text{m}$  diameter PD, the nonlinear effect of both carrier transit-time and impedance could contribute AM-to-PM conversion.

## 2. Structure of MUTC-PDs

The epitaxial layers of our MUTC-PD were grown on an InP substrate, as shown in Fig. 1. From bottom to top, it is composed of the  $n^+$ -InP n-contact layer, n lightly doped InP drift layer, n-doped InP cliff layer, n lightly doped InGaAsP quaternary bandgap “smooth” layer, n lightly doped InGaAs absorption layer, graded p-doped un-depleted InGaAs absorption layer,  $p^+$  doped InGaAsP quaternary bandgap “smooth” layer,  $p^+$  InP electron blocking layer, and  $p^+$  InGaAs p-contact layer. The depletion region includes a 150-nm-thick narrow bandgap absorbing region and a 980-nm-thick wide bandgap non-absorbing region. The InGaAs absorption layer with a graded doping profile is designed to create a quasi-electric field so as to accelerate the electron transport. A 50 nm-thick n-doped InP cliff layer is inserted in the InP drift layer to enhance the electrical field in the depleted absorber layer [20], which facilitates electron transportation at the heterojunction interface, especially under high photocurrent. The MUTC-PDs with diameters 20  $\mu\text{m}$  and 40  $\mu\text{m}$  were processed with standard photolithography and dry etching process and

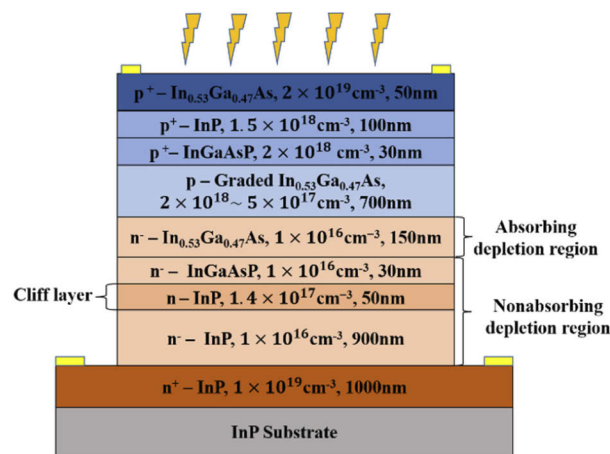
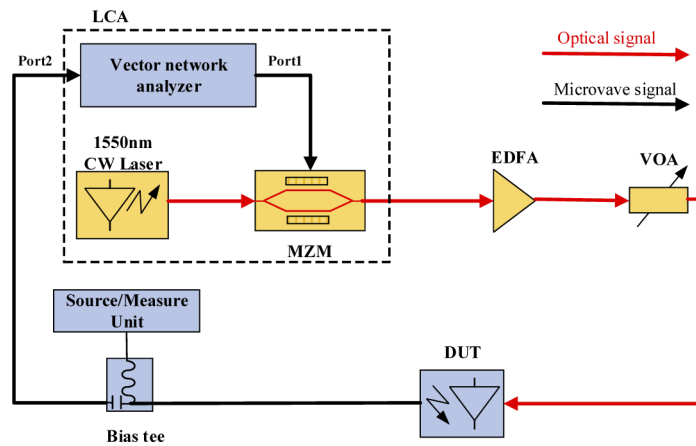


**Fig. 1.** Schematic cross-section of the MUTC-PD.

characterized. At a bias voltage of  $-5\text{V}$ , the dark currents of the MUTC-PDs are less than  $0.17\ \mu\text{A}$ , and the responsivity is about  $0.35\ \text{A/W}$  at  $1550\ \text{nm}$  wavelength without anti-reflection coating for the front-illumination device.

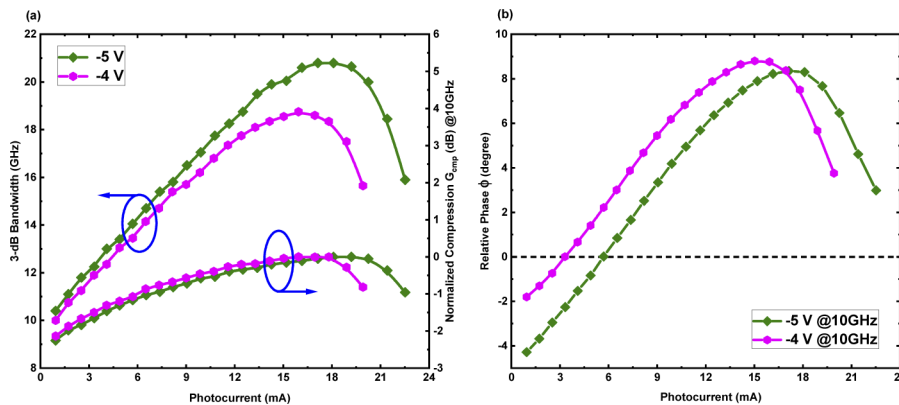
### 3. Experiment setup and measurement results

Figure 2 shows the schematic diagram of the experimental setup to measure S-parameter with the LCA (Keysight N4373D). The EDFA and a mechanical VOA were used to vary the optical power launched into the device under test (DUT), where the DUT was mounted on a thermal-electric cooler with the temperature maintained at  $20\ ^\circ\text{C}$ .



**Fig. 2.** Experimental setup to measure PD's amplitude and phase response. LCA: lightwave component analyzer; MZM: Mach-Zehnder modulator; EDFA: erbium-doped fiber amplifier; VOA: mechanical variable optical attenuator.

The 3-dB bandwidth ( $f_{3\text{dB}}$ ), output RF power compression and relative phase change  $\phi$  of the  $20\ \mu\text{m}$  PD and  $40\ \mu\text{m}$  PD at various photocurrents are plotted in Fig. 3 and Fig. 4, respectively. Here the RF power compression is defined as the deviation of the measured output RF power from the ideal linear output and is given by  $G_{\text{cmp}}[\text{dB}] = P_{\text{out}}[\text{dBm}] - P_{\text{ideal}}[\text{dBm}]$ , where  $G_{\text{cmp}}$  is the RF power compression,  $P_{\text{out}}$  and  $P_{\text{ideal}}$  is the output RF power and the ideal RF power under



**Fig. 3.** (a) The measured 3-dB bandwidth and output RF power compression, and (b) relative phase at 10 GHz versus photocurrent for the  $20\ \mu\text{m}$  PD.

certain photocurrent, respectively. In Fig. 3 and 4, the compression  $G_{\text{cmp}}$  is normalized to the maximum value [16]. As shown in Fig. 3(a) and Fig. 4(a), the trends of  $f_{3\text{dB}}$  and  $G_{\text{cmp}}$  curves vary with photocurrent very similarly under different reverse bias. Along with the increase of photocurrent, firstly the  $f_{3\text{dB}}$  increases to peak value and the  $G_{\text{cmp}}$  approaches 0 dB, after that the  $f_{3\text{dB}}$  decreases and the  $G_{\text{cmp}}$  drops. For the 20  $\mu\text{m}$  diameter device and under bias of  $-5\text{ V}$ , the  $f_{3\text{dB}}$  reaches a maximum value of 20.8 GHz at photocurrent of 18.1 mA, while for the 40  $\mu\text{m}$  diameter device, the peak  $f_{3\text{dB}}$  is 11.2 GHz at 33.1 mA. Because of larger diameter, the 40  $\mu\text{m}$  PD shows lower bandwidth and larger photocurrent before reaching compression. Figure 3(b) and Fig. 4(b) show how the relative phase varies with photocurrent for both devices. It is noted that the 3-dB bandwidth, RF compression value and relative phase reach the peak value at almost the same photocurrent under various reverse biases for both devices.

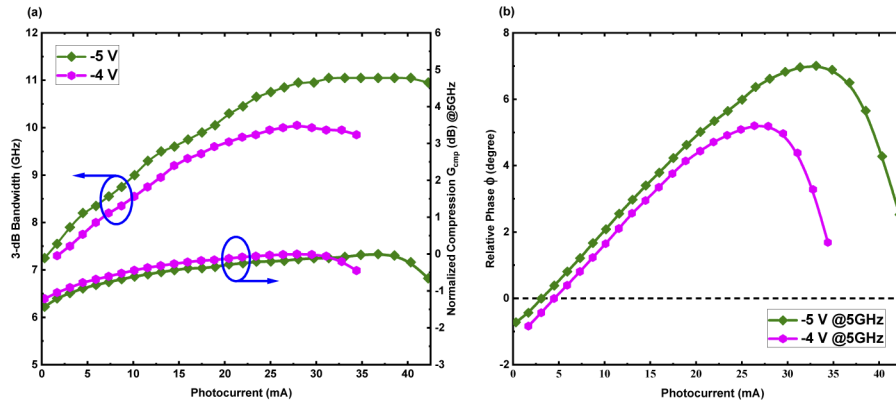


**Fig. 4.** (a) The measured 3-dB bandwidth and output RF power compression, and (b) relative phase at 5 GHz versus photocurrent for the 40  $\mu\text{m}$  PD.

## 4. Analysis and discussion

### 4.1. Bandwidth and phase response

In order to investigate the origin of AM-to-PM conversion, we study the influences of carrier transit-time and impedance on bandwidth and phase at various photocurrents with the equivalent circuit model shown in Fig. 5 in this section. As shown in Fig. 5, region I of the circuit model is composed of a resistor  $R_t$  and a capacitor  $C_t$ , which is used to model the effect of the carrier transit-time, while region II is used to model the device RF impedance. Here in region II, we used a higher order circuit model [21,22], which includes two cascaded resistors ( $R_{j1}$  and  $R_{j2}$ ) and capacitors ( $C_{j1}$  and  $C_{j2}$ ) parallel circuits corresponding to the two depleted regions (depleted absorption region and wide bandgap non-absorption region). Moreover,  $R_3$  represents the bulk resistance which consists of a 700nm undepleted (graded p-doped  $5 \times 10^{17}\text{ cm}^{-3} \sim 2 \times 10^{18}\text{ cm}^{-3}$ ) InGaAs absorption layer, a 30nm p-doped ( $2 \times 10^{18}\text{ cm}^{-3}$ ) InGaAsP quaternary bandgap “smooth” layer and a 100nm p-doped ( $1.5 \times 10^{18}\text{ cm}^{-3}$ ) InP electron blocking layer.  $R_4$  represents the p- and n-contact resistance.  $C_p$  is the p-electrode parasitic capacitance.  $L_c$  and  $C_c$  are the inductance and capacitance of the metallic co-planar waveguide pad, respectively. All these parameters in the circuit model can be extracted by fitting the experimental measured  $S_{22}$  and  $S_{21}$  data of photodiodes with different photocurrents and reverse biases. As shown in Fig. 6, the  $S_{22}$  and  $S_{21}$  parameters are fitted very well with experimental data in the frequency range from 50 MHz to 40 GHz at each photocurrent value.

Given the excellent fitting in Fig. 6, the impedance RC-limited 3-dB bandwidth ( $f_{z,\text{model}}$ ), carrier transit time limited 3-dB bandwidth ( $f_{\text{tr},\text{model}}$ ) and total 3-dB bandwidth ( $f_{\text{tot},\text{model}}$ ) can be

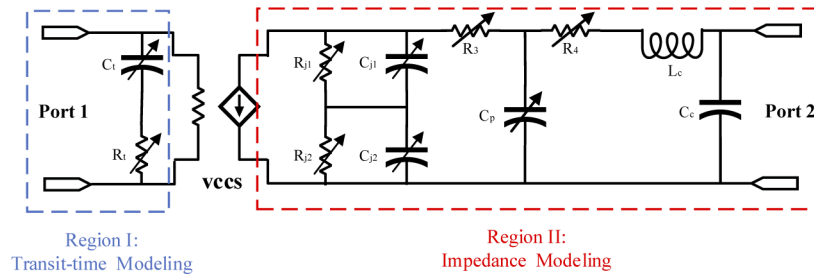


**Fig. 5.** Schematic diagram of the circuit model of the MUTC-PD, VCCS: voltage-controlled current source.

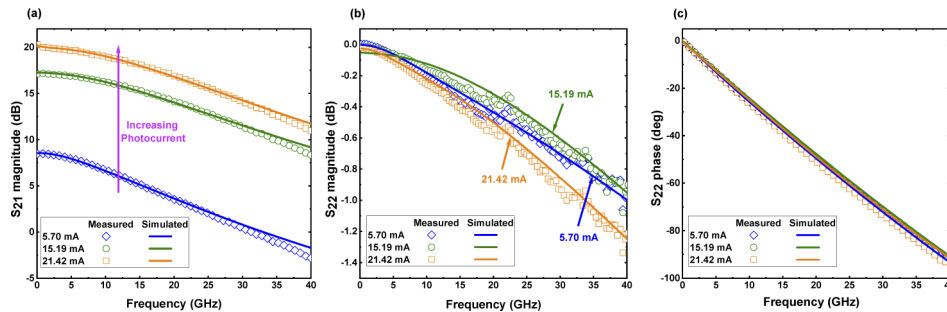


**Fig. 6.** Measured (symbol markers) and simulated (solid lines) S parameters of the 20  $\mu\text{m}$  PD at  $-5$  V bias. (a) magnitude of  $S_{21}$ , (b) magnitude of  $S_{22}$ , (c) phase of  $S_{22}$ .

calculated as shown in Fig. 7. It is noted that the total 3dB bandwidth predicted by the circuit model fits well with experimental measured 3dB bandwidth for all these devices with different diameters under various bias and photocurrent conditions. It is also noted that the  $f_{\text{tot,model}}$  of the 20  $\mu\text{m}$  PD is primarily limited by  $f_{\text{tr,model}}$  up to the highest photocurrent measured as shown in Fig. 7(a) and 7(b), while for 40  $\mu\text{m}$  PD, the  $f_{\text{tot,model}}$  is limited by both  $f_{z,model}$  and  $f_{\text{tr,model}}$ . Moreover, as shown in Fig. 7,  $f_{z,model}$  first increases and then decreases as the photocurrent varies. The photocurrent dependent  $f_{z,model}$  is due to the variation of the PDs' impedance as the photocurrent varies [23]. In Fig. 8, the extracted values of the circuit elements are plotted at various photocurrents. In Fig. 8(a), the capacitance  $C_{j1}$  remains almost constant for different photocurrents. However, the capacitance  $C_{j2}$  increases as the photocurrent increases as indicated Fig. 8(b). The changing trend of capacitances ( $C_{j1}$  and  $C_{j2}$ ) is determined by the width of the depletion region, which will be confirmed in electric field analysis later. Figure 8(c) shows the extracted values of the resistance  $R_3$  at various photocurrents for the 20  $\mu\text{m}$  PD and the 40  $\mu\text{m}$  PD. Moreover, the parameter  $C_p$  in the circuit model does not change significantly as the photocurrent varies and the parameters  $R_4$ ,  $L_c$  and  $C_c$  do not change as the photocurrent increases. In our front-illuminated PDs with ring electrodes, the nonlinearities of  $f_{z,model}$  can be mainly attributed to the resistance  $R_3$  [24], while other circuit parameters in Region II can also influence the  $f_{z,model}$ . The value of the resistance  $R_3$  is dependent on the potential drop and spatial distribution of the carriers. As shown in Fig. 8(c), the value of  $R_3$  first decreases, which implies a reduction in the time constant of the impedance, leading to an improvement in the  $f_{z,model}$ . When the photocurrent is further increases, the value of  $R_3$  tends to increase. In Fig. 8(c), for the 20  $\mu\text{m}$  PD under a bias voltage of  $-5$  V, the value of  $R_3$  first decreases from 142  $\Omega$  to 0.8  $\Omega$  as the photocurrent increases from 5.7 mA to 15.5 mA and then increases when the photocurrent further increases. This behavior is very similar to  $f_{z,model}$  behavior as shown in

Fig. 7. The increase of  $R_3$  at large photocurrent may be due to load effect, which increases the potential drop.

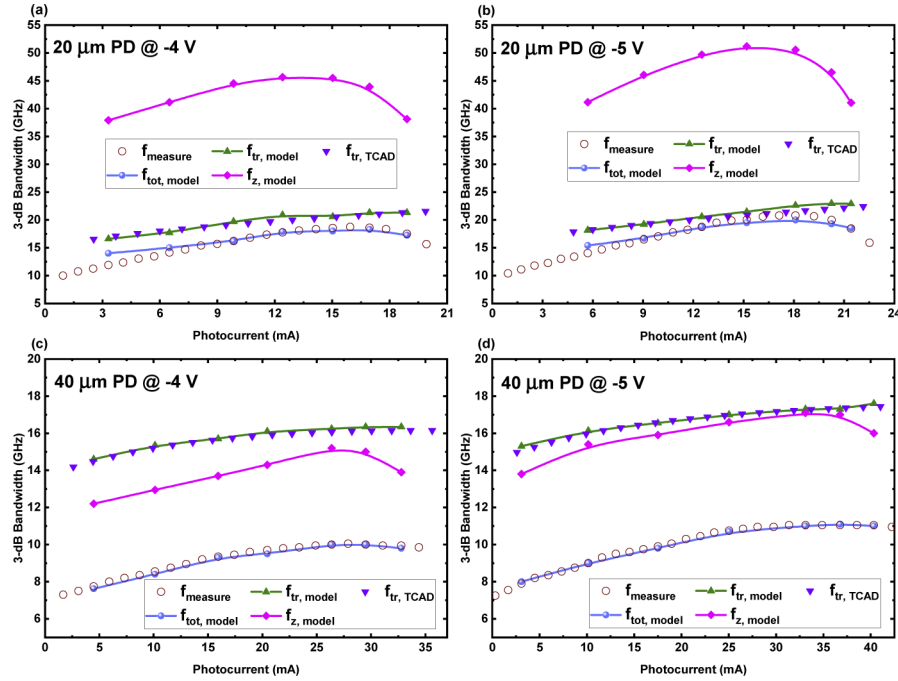


Fig. 7. The measured, simulated transit-time-limited, impedance RC-limited, total, and TCAD-simulated bandwidth of the 20  $\mu\text{m}$  PD under (a) -4 V bias, (b) -5 V bias, and the 40  $\mu\text{m}$  PD under (c) -4 V bias, (d) -5 V bias versus photocurrent. (model: circuit model).

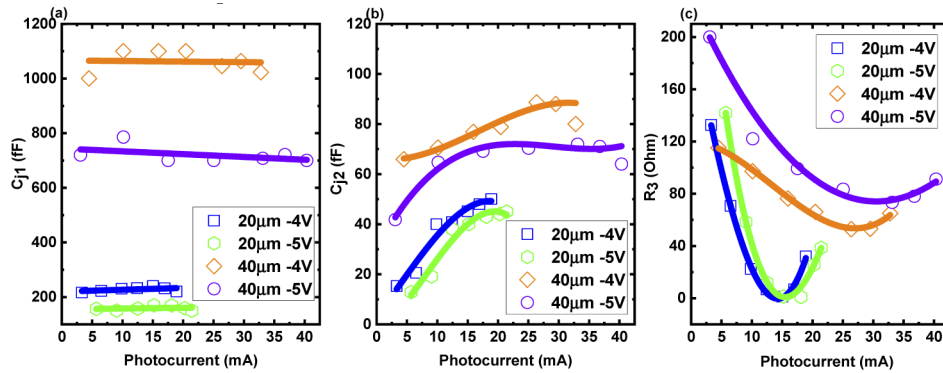
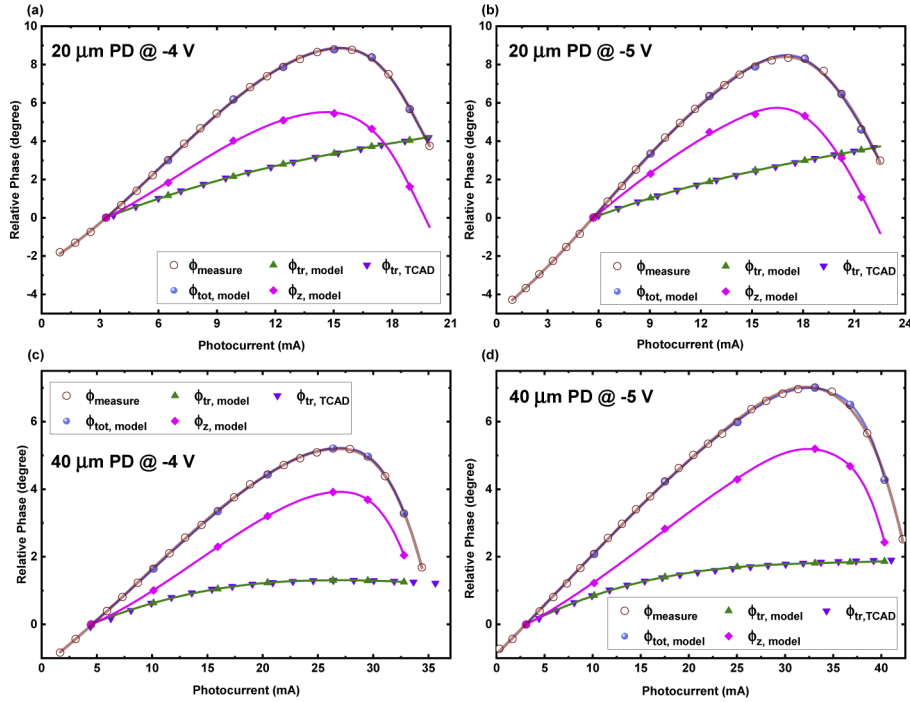


Fig. 8. Extracted (a) capacitance  $C_{j1}$ , (b) capacitance  $C_{j2}$  and (c) resistance  $R_3$  versus photocurrents under different reverse biases for the 20  $\mu\text{m}$  PD and 40  $\mu\text{m}$  PD. The solid lines are fitting results using the symbol markers.

We used the same equivalent circuit to extract the relative phase at different photocurrents. The carrier transit time limited, impedance RC-limited, and total relative phases of the 20  $\mu\text{m}$  PD and 40  $\mu\text{m}$  PD are plotted in Fig. 9. The trend of the relative phase  $\phi_{z,model}$  is very similar to  $f_{z,model}$ . As shown in Fig. 9,  $\phi_{z,model}$  first increases and then decreases. In Fig. 9(a) and 9(b), for 20  $\mu\text{m}$  PD the  $\phi_{z,model}$  peaks at a slightly different photocurrent from that of total phase  $\phi_{tot,model}$ ,

since the contribution of  $\phi_{tr,model}$  is more significant in the PD with small diameter. However, for 40  $\mu\text{m}$  PD, it is noted that the  $\phi_{z,model}$  dominates the relative phase  $\phi_{tot,model}$ , and they peak at the same photocurrent value.



**Fig. 9.** The measured, simulated transit-time-limited, impedance RC-limited, total, and TCAD-simulated relative phase responses of the 20  $\mu\text{m}$  PD at 10 GHz under (a)  $-4$  V bias, (b)  $-5$  V bias and the 40  $\mu\text{m}$  PD at 5 GHz under (c)  $-4$  V bias, (d)  $-5$  V bias versus photocurrent. The symbol markers are measured and simulated data, and the solid lines are the corresponding fitting curves using the symbol markers. (model: circuit model).

In order to further verify the accuracy of region I in the circuit model, Silvaco TCAD model based on the drift-diffusion equation was used to study both the carrier transit-time limited bandwidth  $f_{tr,TCAD}$  and transit-time induced phase  $\phi_{tr,TCAD}$  as well. It is noted that the transit-time limited bandwidth  $f_{tr,model}$  and transit-time induced phase  $\phi_{tr,model}$  based on the circuit model match very well as that from the TCAD model as indicated in Fig. 7 and Fig. 9. Since propagation speed of the modulated microwave signal depends on the carrier transit velocity and the number of carriers, the transit-time induced phase  $\phi_{tr,TCAD}$  has a similar behavior as the  $f_{tr,TCAD}$  [14]. In the TCAD model, the fundamental reason of how the transit time limited bandwidth  $f_{tr,TCAD}$  changes with photocurrent was uncovered, which is due to the self-induced electric field in the un-depleted absorption layer [16]. This is confirmed by the electric field distribution of the PD at different photocurrents in Fig. 10. As shown in the inset of Fig. 10, in the un-depleted absorption region, the self-induced electric field increases with the photocurrent. Moreover, it is found in Fig. 10, the high electric field in the InGaAs depleted absorption region remains at high photocurrent, therefore the capacitance  $C_{j1}$  remains almost constant for different photocurrents. However, the collapse of the electric field in the InP drift region takes place as the photocurrent increases, which explains the phenomena that the capacitance  $C_{j2}$  increases as the photocurrent increases as shown in Fig. 8(b).

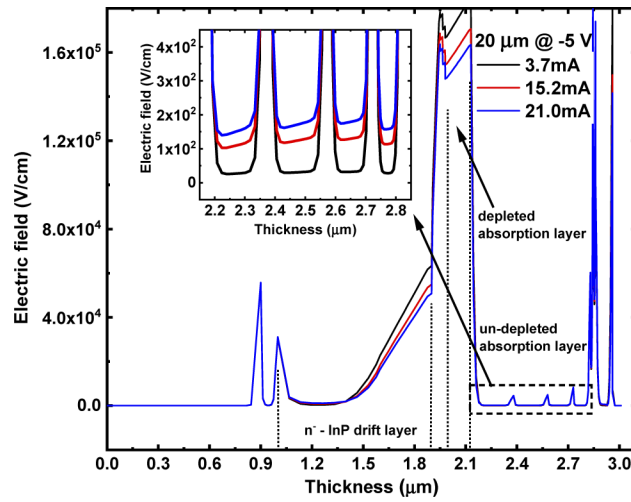


**Fig. 10.** Distribution of electric field in the 20  $\mu\text{m}$  PD under  $-5\text{ V}$  bias at different photocurrents.

#### 4.2. AM-to-PM conversion

The AM-to-PM conversion coefficient  $\alpha$  is used to characterize the amplitude-variation-induced phase change, which is define as below. Here  $\Delta\phi$  is the phase change caused by the relative

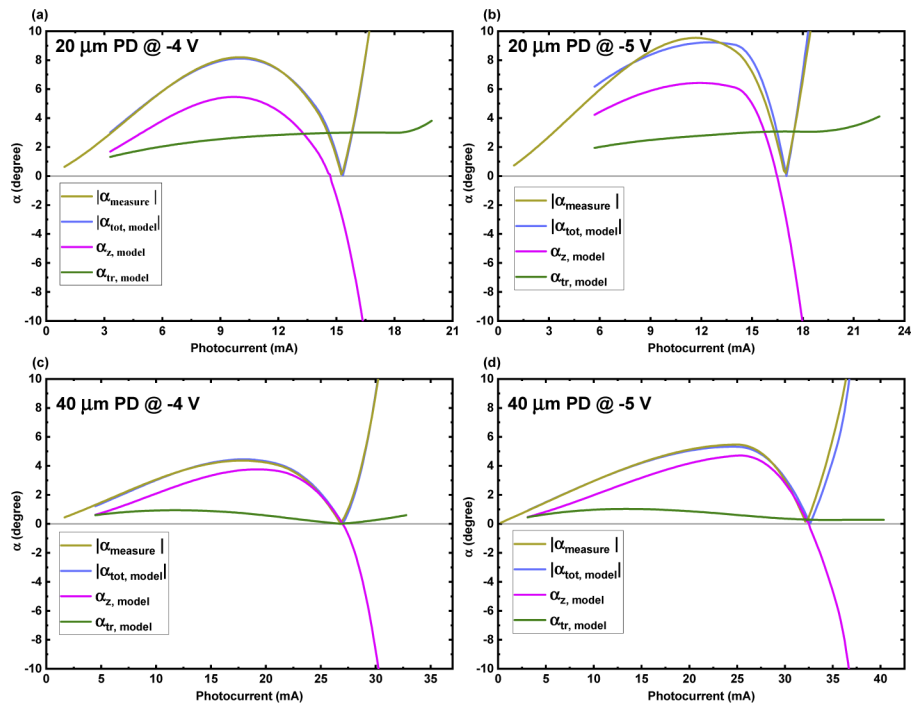


**Fig. 11.** Calculated AM-to-PM conversion coefficient versus photocurrent for the 20  $\mu\text{m}$  PD at 10 GHz under (a)  $-4\text{ V}$  bias, (b)  $-5\text{ V}$  bias and the 40  $\mu\text{m}$  PD at 5 GHz under (c)  $-4\text{ V}$  bias, (d)  $-5\text{ V}$  bias. (model: circuit model).

optical power ( $\Delta P/P$ ) or photocurrent ( $\Delta I/I$ ) variation.

$$\alpha = \frac{\Delta\phi}{\Delta P/P} = \frac{\Delta\phi}{\Delta I/I} \quad (1)$$

Moreover, we can separate the total phase change into two parts, one is the phase change due to carrier transit time variation  $\Delta\phi_{tr}$ , the other is the phase change due to the impedance variation  $\Delta\phi_z$ . Similarly, we can also define the corresponding AM-to-PM conversion coefficient  $\alpha_{tr}$  and  $\alpha_z$ , and the total AM-to-PM conversion coefficient is the sum of  $\alpha_{tr}$  and  $\alpha_z$ .

Figure 11 shows the results of the AM-to-PM conversion coefficients due to different mechanisms. These simulated results  $|\alpha_{tot,model}|$  agree with the experimental results very well. As shown in Fig. 11(a), for 20  $\mu\text{m}$  PD, the “null” point of  $\alpha_{z,model}$  occurs at 14.66 mA under  $-4\text{V}$  bias, which is 0.59 mA lower than the “null” point of  $|\alpha_{measure}|$ , similarly, at  $-5\text{V}$  as indicated in Fig. 11(b). The difference between the “null” point of  $\alpha_{z,model}$  and the “null” point of  $|\alpha_{measure}|$  is due to the contribution from  $\alpha_{tr,model}$  for the 20  $\mu\text{m}$  PD, where the internal transit-time contributes to the total phase increase and pull the “null” point to a higher photocurrent. In contrast, for the 40  $\mu\text{m}$  PD, the “null” points of  $\alpha_{z,model}$  and  $|\alpha_{measure}|$  match very well, which indicates that impedance induced AM-to-PM conversion dominates for the device with large size.

## 5. Conclusion

We have measured and studied the AM-to-PM conversion in MUTC-PDs for the 20  $\mu\text{m}$  and 40  $\mu\text{m}$  diameters. A photocurrent-dependent equivalent circuit considering both carrier transit-time and impedance effects was developed to model AM-to-PM conversion. It is found that the AM-to-PM conversion for 40  $\mu\text{m}$  PD is mainly induced by the impedance change as photocurrent varies, while for 20  $\mu\text{m}$  PD, both carrier transit-time and impedance should be considered for the AM-to-PM conversion. These analyses suggest that the nonlinearity performance of the photocurrent-dependent impedance is critical and should be taken into account for the AM-to-PM conversion.

**Funding.** National Key Research and Development Program of China (2019YFB2203400).

**Acknowledgments.** We are grateful to the device fabrication support from the ShanghaiTech University Quantum Device Lab.

**Disclosures.** The authors declare no conflicts of interest.

**Data availability.** Data underlying the results presented in this paper are not publicly available at this time but may be obtained from the authors upon reasonable request.

## References

1. D. Zhu, C. Yang, Z. Cao, and X. Li, “Measuring the Residual Phase Noise of Photodiodes Using Two-Tone Correlation Method,” *IEEE Photon. Technol. Lett.* **26**(22), 2264–2266 (2014).
2. X. S. Yao and L. Maleki, “Optoelectronic microwave oscillator,” *J. Opt. Soc. Am. B* **13**(8), 1725–1735 (1996).
3. P. Ghelfi, F. Laghezza, F. Scotti, G. Serafino, A. Capria, S. Pinna, D. Onori, C. Porzi, M. Scaffardi, A. Malacarne, V. Vercesi, E. Lazzeri, F. Berizzi, and A. Bogoni, “A fully photonics-based coherent radar system,” *Nature* **507**(7492), 341–345 (2014).
4. G. C. Valley, “Photonic analog-to-digital converters,” *Opt. Express* **15**(5), 1955–1982 (2007).
5. C. Mukherjee, M. Natrella, J. Seddon, C. Graham, P. Mounaix, C. C. Renaud, and C. Maneux, “Efficient compact modelling of UTC-photodiode towards terahertz communication system design,” *Solid State Electron.* **170**(107836), 107836 (2020).
6. Z. Naseem, R. L. Ahmad, H. S. Chao, C. J. Chang, H. S. Ni, J. J. Chen, E. Huang, Y. H. Chou, J. W. Jan, and Shi, “Enhancement in speed and responsivity of uni-traveling carrier photodiodes with  $\text{GaAs}_{0.5}\text{Sb}_{0.5}/\text{In}_{0.53}\text{Ga}_{0.47}\text{As}$  type-II hybrid absorbers,” *Opt. Express* **27**(11), 15495–15504 (2019).
7. Y. Hu, C. R. Menyuk, X. Xie, M. N. Hutchinson, V. J. Urlick, J. C. Campbell, and K. J. Williams, “Computational Study of Amplitude-to-Phase Conversion in a Modified Unitraveling Carrier Photodetector,” *IEEE Photonics J.* **9**(2), 1–11 (2017).
8. J. Taylor, S. Datta, A. Hati, C. Nelson, F. Quinlan, A. Joshi, and S. Diddams, “Characterization of Power-to-Phase Conversion in High-Speed P-I-N Photodiodes,” *IEEE Photonics J.* **3**(1), 140–151 (2011).

9. J. Zang, X. Xie, Q. Yu, Z. Yang, A. Beling, and J. C. Campbell, "Reduction of Amplitude-to-Phase Conversion in Charge-Compensated Modified Unitraveling Carrier Photodiodes," *J. Lightwave Technol.* **36**(22), 5218–5223 (2018).
10. T. M. Fortier, F. Quinlan, A. Hati, C. Nelson, J. A. Taylor, Y. Fu, J. Campbell, and S. A. Diddams, "Photonic microwave generation with high-power photodiodes," *Opt. Lett.* **38**(10), 1712–1714 (2013).
11. J. Sun, B. Xu, W. Sun, S. Zhu, and N. Zhu, "The Effect of Bias and Frequency on Amplitude to Phase Conversion of Photodiodes," *IEEE Photonics J.* **12**(4), 1–10 (2020).
12. J. Davila-Rodriguez, X. Xie, J. Zang, C. J. Long, T. M. Fortier, H. Leopardi, T. Nakamura, J. C. Campbell, S. A. Diddams, and F. Quinlan, "Optimizing the linearity in high-speed photodiodes," *Opt. Express* **26**(23), 30532–30545 (2018).
13. W. Zhang, W. Zhang, T. Li, T. Li, M. Lours, M. Lours, S. Seidelin, S. Seidelin, G. Santarelli, G. Santarelli, Y. Le Coq, and Y. Le Coq, "Amplitude to phase conversion of InGaAs pin photo-diodes for femtosecond lasers microwave signal generation," *Appl. Phys. B* **106**(2), 301–308 (2012).
14. D. Eliyahu, D. Seidel, and L. Maleki, "RF amplitude and phase-noise reduction of an optical link and an opto-electronic oscillator," *IEEE Trans. Microwave Theory Techn.* **56**(2), 449–456 (2008).
15. L. Kang and B. H. Kolner, "Characterization of AM-to-PM Conversion in Silicon p-i-n Photodiodes," *IEEE Photon. Technol. Lett.* **31**(13), 1001–1004 (2019).
16. X. Xie, J. Zang, A. Beling, and J. Campbell, "Characterization of amplitude noise to phase noise conversion in charge-compensated modified unitravelling carrier photodiodes," *J. Lightwave Technol.* **35**(9), 1718–1724 (2017).
17. J. -M. Wun, Y. -W. Wang, and J. -W. Shi, "Ultrafast Uni-Traveling Carrier Photodiodes With GaAs<sub>0.5</sub>Sb<sub>0.5</sub>/In<sub>0.53</sub>Ga<sub>0.47</sub>As Type-II Hybrid Absorbers for High-Power Operation at THz Frequencies," *IEEE J. Sel. Top. Quant.* **24**(2), 1–7 (2018).
18. T. M. Fortier, M. S. Kirchner, F. Quinlan, J. Taylor, J. C. Bergquist, T. Rosenband, N. Lemke, A. Ludlow, Y. Jiang, C. W. Oates, and S. A. Diddams, "Generation of ultrastable microwaves via optical frequency division," *Nat. Photonics* **5**(7), 425–429 (2011).
19. D. Yang, Y. Huang, X. Duan, K. Liu, Y. Yang, and X. Ren, "The Tunable Phase Shift of High-Speed PIN Photodetector and Modified Uni-Traveling Carrier Photodetector," *J. Lightwave Technol.* **39**(6), 1873–1879 (2021).
20. Z. Li, H. Pan, H. Chen, A. Beling, and J. C. Campbell, "High-Saturation-Current Modified Uni-Traveling-Carrier Photodiode With Cliff Layer," *IEEE J. Quantum Elect.* **46**(5), 626–632 (2010).
21. J. Li, B. Xiong, C. Sun, D. Miao, and Y. Luo, "Analysis of frequency response of high power MUTC photodiodes based on photocurrent-dependent equivalent circuit model," *Opt. Express* **23**(17), 21615–21623 (2015).
22. M. Natrella, C. Liu, C. Graham, F. van Dijk, H. Liu, C. C. Renaud, and A. J. Seeds, "Accurate equivalent circuit model for millimetre-wave UTC photodiodes," *Opt. Express* **24**(5), 4698–4713 (2016).
23. J. Shi, F. M. Kuo, C. Yang, S. S. Lo, and C. Pan, "Dynamic Analysis of Cascaded Laser Power Converters for Simultaneous High-Speed Data Detection and Optical-to-Electrical DC Power Generation," *IEEE T. Electron Dev.* **58**(7), 2049–2056 (2011).
24. X. Li, N. Li, S. Demiguel, J. C. Campbell, D. Tulchinsky, and K. J. Williams, "A comparison of front- and backside-illuminated high-saturation power partially depleted absorber photodetectors," *IEEE J. Quantum Elect.* **40**(9), 1321–1325 (2004).